nature neuroscience

Coherent neuronal ensembles are rapidly recruited when making a look-reach decision

Yan T Wong[1,3], Margaret M Fabiszak[1], Yevgeny Novikov[1], Nathaniel D Daw[1–3] & Bijan Pesaran[1]

Selecting and planning actions recruits neurons across many areas of the brain, but how ensembles of neurons work together to make decisions is unknown. Temporally coherent neural activity may provide a mechanism by which neurons coordinate their activity to make decisions. If so, neurons that are part of coherent ensembles may predict movement choices before other ensembles of neurons. We recorded neuronal activity in the lateral and medial banks of the intraparietal sulcus (IPS) of the posterior parietal cortex while monkeys made choices about where to look and reach. We decoded the activity to predict the choices. Ensembles of neurons that displayed coherent patterns of spiking activity extending across the IPS—'dual-coherent' ensembles—predicted movement choices substantially earlier than other neuronal ensembles. We propose that dual-coherent spike timing reflects interactions between groups of neurons that are important to decisions.

Voluntary movements such as looking and reaching are controlled by distributed networks containing millions of neurons. The brain areas associated with voluntary movements are organized into effector-specific networks specialized for the control of each movement. There is a network for controlling saccadic eye movements and a network for controlling transport movements of the arm, along with other networks that control the hand. Evidence from electrophysiological and functional neuroimaging experiments supports the idea that eye and arm movement systems are controlled by different brain networks[1–4]. Effector-specific networks are widespread and extend across the frontal and parietal cortices[5–7], basal ganglia[8], association nuclei of the thalamus[9], and cerebellum[10].

A great deal is known about how neurons in effector-specific networks are recruited when we make decisions. In the posterior parietal cortex (PPC), neurons on the lateral bank of the intraparietal sulcus (IPS), including the lateral intraparietal area (area LIP), tend to respond before eye movements, while neurons on the medial bank (including the parietal reach region, medial intraparietal area (MIP) and ventral area 5) tend to respond before arm movements[11,12]. Neural activity in PPC of macaques encodes which of multiple alternatives will be chosen, which effector will be used to make the choice and other decision-related variables[13–16]. PPC neurons play a causal role in effector-specific choice. Reversibly inactivating the PPC disrupts movement coordination, selection and decision-making, and it does so in an effector-based manner[17–20]. Functional neuroimaging experiments indicate that the human parietal cortex also has a similar effector-specific organization[3,4,21]. Therefore, largely different networks of neurons are believed to be involved in selecting where to move the eyes and where to move the arm.

Relatively little is known about the interactions between PPC neurons and how making a look-reach decision depends on these interactions. Coherent neural activity is broadly present within the intraparietal sulcus of the PPC[22,23] and has been implicated in a wide range of cognitive processes[24,25], including decision making[26–28], working memory[29,30], movement planning and execution[22,31,32], and attention[33,34]. Therefore, a relationship between coherent neural activity in PPC and effector-based decision-making is likely, and knowledge of such neuronal interactions may provide new opportunities to test models of how look-reach decisions are made.

We recorded neural activity simultaneously from electrodes in both the lateral and medial banks of the IPS while monkeys chose to make a coordinated look-and-reach to one of two locations. Coordinated movements are likely to recruit neuronal ensembles on both banks, so we used coherence to identify groups of distributed, interacting neurons. We then compared how neuronal ensembles were recruited when making a decision by estimating when the firing of neurons correctly predicted the movement choice. The results show that deciding where to look and reach recruits dual-coherent patterns of neuronal activity and inform models of how effector-specific networks of neurons make look-reach decisions.

RESULTS

We recorded neurons and LFP activity from the lateral and medial banks of the IPS in two monkeys (**Fig. 1a**). Of the neurons recorded, 117 displayed persistent, spatially selective responses before a reach-and-saccade movement (center-out task), as well as in a choice task that required them to choose where to look and reach (**Fig. 1b**). These included 47 neurons from the lateral bank of the IPS (monkey C, 30; monkey R, 17) and 70 neurons from the medial bank (C, 45; R, 25). Individual neurons on both banks of the IPS (**Fig. 1c**,**d**), as well as the population average (**Fig. 1e**,**f**), robustly responded to the onset of the targets and signaled the choice during an instructed delay before movement, consistent with the formation of movement plans.

[1]Center for Neural Science, New York University, New York, New York, USA. [2]Psychology Department, New York University, New York, New York, USA. [3]Present addresses: Electrical and Electronic Engineering, University of Melbourne, Parkville, Victoria, Australia (Y.T.W.) and Psychology Department and Princeton Neuroscience Institute, Princeton University, Princeton, New Jersey, USA (N.D.D.). Correspondence should be addressed to B.P. (bijan@nyu.edu).

Received 10 September 2015; accepted 1 December 2015; published online 11 January 2016; doi:10.1038/nn.4210

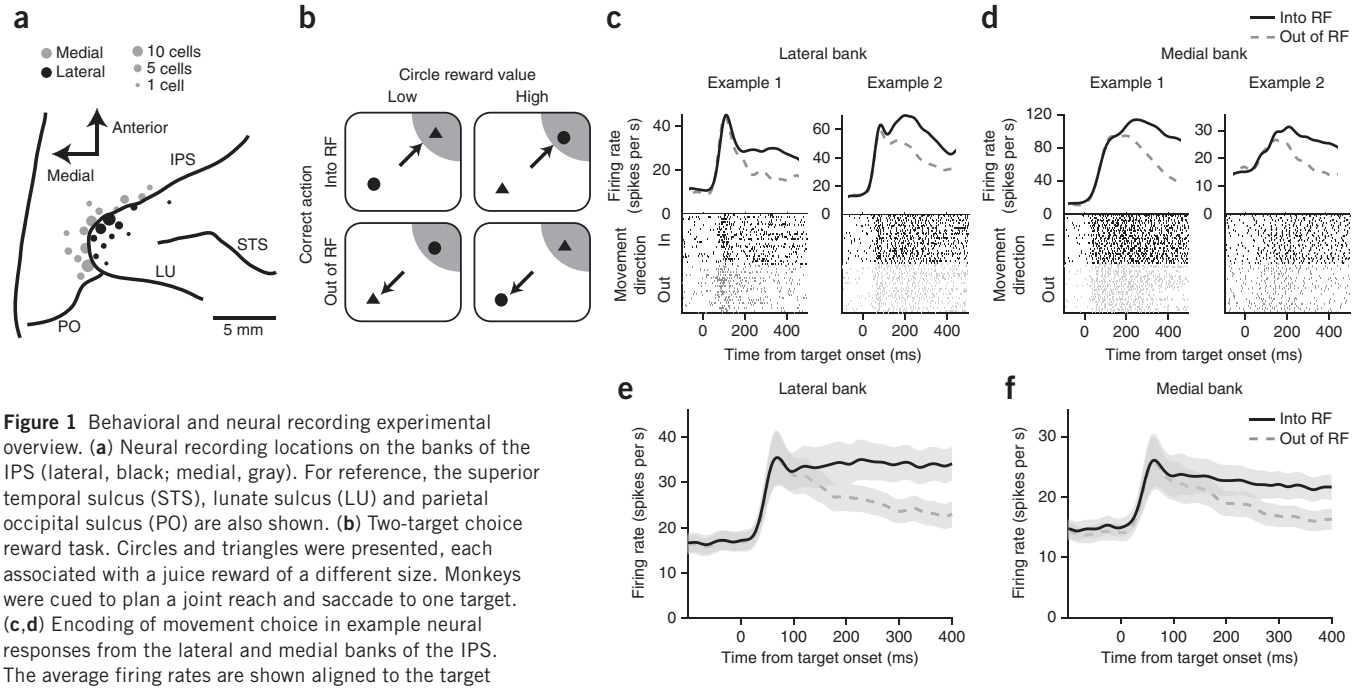

Figure 1 Behavioral and neural recording experimental overview. (**a**) Neural recording locations on the banks of the IPS (lateral, black; medial, gray). For reference, the superior temporal sulcus (STS), lunate sulcus (LU) and parietal occipital sulcus (PO) are also shown. (**b**) Two-target choice reward task. Circles and triangles were presented, each associated with a juice reward of a different size. Monkeys were cued to plan a joint reach and saccade to one target. (**c**,**d**) Encoding of movement choice in example neural responses from the lateral and medial banks of the IPS. The average firing rates are shown aligned to the target presentation. Solid black lines denote movements into the RF; dashed gray lines denote movements out of the RF. (**e**,**f**) Population average firing rates for the lateral bank (**e**) and medial bank (**f**). The s.e.m. of the firing rates is shaded in gray.

Long-range and local spike-field coherence

Selection may depend on the presence of coherent patterns of neuronal activity. We first asked whether ensembles of neurons exist that are coherently active across the IPS. To do so, we analyzed correlations between spiking and LFP activity using spike-field coherence (SFC). SFC characterizes correlations in the timing of spiking and LFP activity according to temporal frequency. SFC magnitude measures how well spike times from a particular neuron can be predicted given LFP activity, and consequently it measures which neurons participate in coherent neural ensembles.

We measured SFC on the same bank (local) or on opposite banks (long-range; **Fig. 2a**) of the IPS. We defined local-only coherent neurons as being coherent with local but not long-range LFP activity, long-range-only coherent neurons as being coherent with long-range but not local LFP activity, dual-coherent neurons as being coherent with both long-range and local LFP activity and noncoherent neurons as those that were not coherent with local or long-range LFPs.

Seventy-two neurons were recorded with LFP activity from electrodes placed in both banks of the IPS (C, 53; R, 19; 144 unique spike-field pairs). Previous work has shown beta-frequency activity to be specifically recruited during coordinated movements. Our initial analyses also showed that distributed coherence between the two banks of the IPS was consistent and relatively widespread in a beta (15–25 Hz) frequency band. We therefore tested each neuron for significant SFC with local or long-range LFP activity at 20 Hz during the baseline epoch. Thirty neurons were dual-coherent (42%; **Fig. 2**), 23 were local-only coherent (32%), 6 were long-range-only coherent (8%), and 13 were noncoherent (18%). The SFC phase between local (−38.2 ± 20.6°) and long-range (19.4 ± 19.5°) LFP activity differed for dual-coherent neurons ($P = 0.01$, rank-sum test), indicating that the LFP activity in the two areas differs. Finally, coherence was equally likely in each bank, with the proportion of locally coherent medial neurons not significantly different from that of the whole population ($P = 0.11$, binomial test).

Dual-coherent neurons signal choices first

Selecting a look-and-reach movement plan may involve communication between different effector-specific networks, preferentially recruiting dual-coherent ensembles that extend between the banks of the IPS. If coherent ensembles are involved in selecting the plan, dual-coherent neurons should start to signal movement plans earlier than other groups of neurons.

After the onset of the choice targets, firing rates of dual-coherent neurons before movements into and out of the response field (RF) separated substantially earlier than the firing rates of both local-only and noncoherent neurons (dual, 45 ms; local, 112 ms; noncoherent, 107 ms; **Fig. 3a**,**b**). Firing rates of long-range-only coherent neurons did not become significantly different before the movement.

The separation in firing rates indicates that dual-coherent neurons predict choices before the other populations. To quantify choice information moment by moment, we performed a receiver operating characteristic (ROC) analysis. The dual-coherent neurons had a significantly higher values for the area under the ROC curve (AUC) than local-only and noncoherent neurons (dual, 0.55 ± 0.01; local, 0.51 ± 0.01; noncoherent, 0.51 ± 0.01, 75 ms after target onset; **Fig. 3c**; false discovery rate–corrected rank-sum test, $P < 0.05$). We performed this analysis at a population level by averaging trials from 12 randomly selected neurons. The AUC values were also different from chance (0.5) earlier for dual-coherent neurons than other groups (dual, 55 ms; local, 92 ms; noncoherent, 109 ms; **Fig. 3d**).

Fewer long-range-only coherent neurons were recorded, so we recalculated the ROC analysis using smaller populations of neurons in order to compare all four populations ($n = 5$; **Supplementary Fig. 1a**,**b**). The properties of dual, local-only and noncoherent neurons remained consistent, with long-range-only neuron firing rates separating the slowest.

The above analyses show that dual-coherent neurons are selective earlier than other groups of neurons. However, the analyses involved setting an arbitrary detection threshold. To control for this,

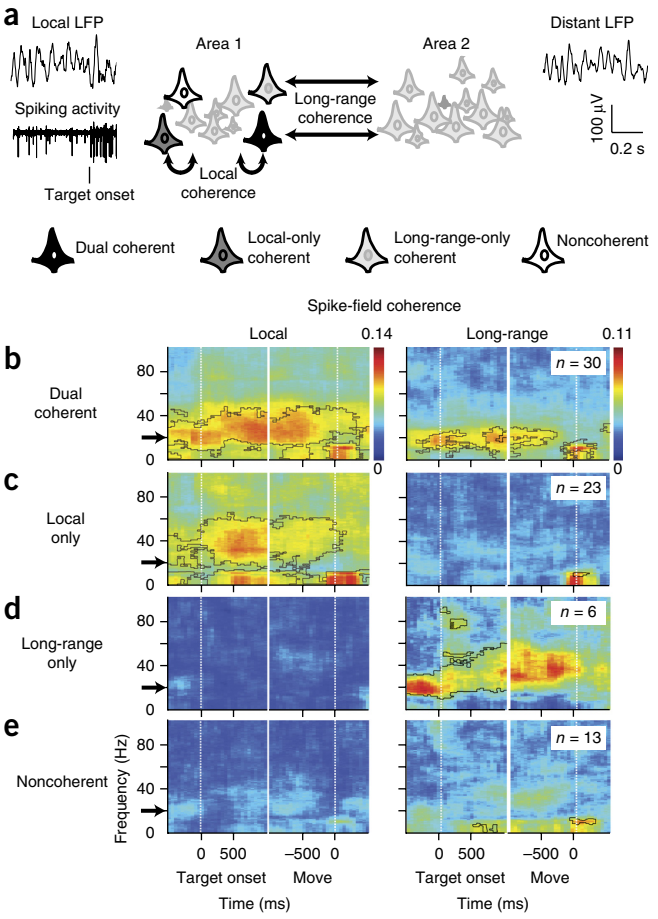

Figure 2 Spike field classification of neurons. (**a**) Each neurons was classified on the basis of whether its spiking activity was coherent with a local LFP in the same area or a distant LFP in the adjacent area (permutation test, cluster-corrected for multiple comparisons; $P < 0.05$, 5 Hz smoothing). (**b**–**e**) Neurons with both local and long-range coherence are referred to as dual-coherent (**b**), with only local coherence as local-only coherent (**c**), with only long-range as long-range-only coherent (**d**), and without any coherence as noncoherent (**e**). For classification, SFC was tested in the beta band before presentation of the target onset cue. The local and long-range coherence for each subpopulation is shown, with areas of significance highlighted in black.

we employed an approach from signal detection theory, the accumulated log-likelihood ratio (AccLLR) method[23], that does not rely on an arbitrary detection threshold and explicitly reveals and controls for the speed–accuracy trade-off (**Fig. 4a**,**b**). On each trial, neural activity for movements into or out of the RF was converted into a log-likelihood ratio that then accumulated in time. The selection time (ST) was defined by the time at which the activity reached a threshold (**Fig. 4a**), with the speed–accuracy trade-off set by this threshold (**Fig. 4b**). When the threshold was set low, detection was fast but inaccurate. As the threshold was raised, performance slowed but was more accurate. We estimated the ST while controlling the speed–accuracy trade-off by setting the threshold to the lowest level that gave perfect classification performance (100% correct detections and 0% false alarms). To measure the ST of populations of neurons, we pooled information across neurons and trials. The STs for perfect classification performance saturated and did not decrease below a certain time even when the size of the neuronal ensemble increased. The presence of saturation validated the estimate of ST and indicated that it was a property of the neuronal ensemble being characterized and did not depend on the number of neurons recorded as part of the ensemble[23].

Consistent with earlier analyses, selection times were faster for dual-coherent neurons than for noncoherent neurons (**Fig. 4c** and **Supplementary Fig. 1c**; dual, 205 ± 4 ms; noncoherent, 247 ± 4 ms; $P = 9.6 \times 10^{-10}$, rank-sum test, mean ± s.e.m.). STs for dual-coherent neurons were also faster than for local-only coherent neurons (255 ± 5 ms, $P = 1.3 \times 10^{-10}$). STs for noncoherent neurons were not significantly different from local-only coherent neurons ($P = 0.14$, rank-sum test). The results remained significant when we calculated STs using data from each monkey separately (**Supplementary Fig. 1d**). For the above comparisons, the decoding accuracy was set to 100% (**Fig. 4d**); however, the results remained the same at an 85% decoding accuracy (dual versus local, $P = 5 \times 10^{-4}$; dual versus noncoherent, $P = 7.4 \times 10^{-5}$; rank-sum test).

Coherent neurons may reflect processes that are not specific to decision making, such as visual selectivity. However, the timing of the visual onset was the same for coherent and noncoherent ensembles (dual, 39 ± 3 ms; local, 41 ± 5 ms; noncoherent, 36 ± 3 ms; dual versus local, $P = 0.62$; dual versus noncoherent, $P = 0.45$, local versus noncoherent, $P = 0.23$; rank-sum test). Therefore, coherent activity was

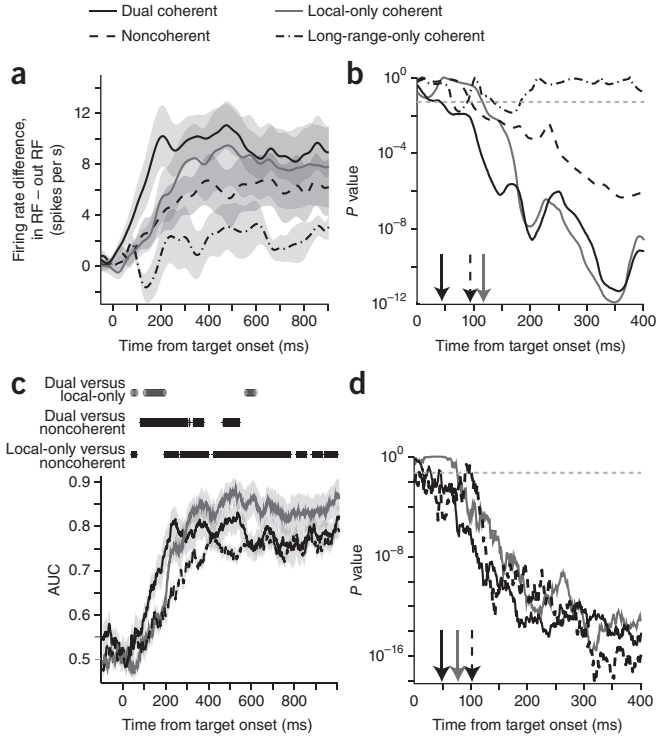

Figure 3 Timing of information in the firing rates of coherent groupings. (**a**) Difference in firing rate for movements into and out of the RF for different groups of neurons. Mean ± s.e.m. are shown. (**b**) *P*-values for a Wilcoxon rank-sum test comparing firing rates into and out of the RF for each group. Arrows indicate the first point the *P*-value fell below 0.05 for three consecutive bins and remained significant. (**c**) AUC values for an ROC analysis on population average firing rates for movements into and out of the RF. Mean ± 95% confidence intervals are shown. The symbols above the AUC lines indicate significant differences between each pair of lines using a false-discovery-rate-corrected Wilcoxon rank-sum test. (**d**) *P*-values for a Wilcoxon rank-sum test comparing the AUC values for each group against 0.5. Arrows indicate the first point the values fell below 0.05 for three consecutive bins and remained significant.

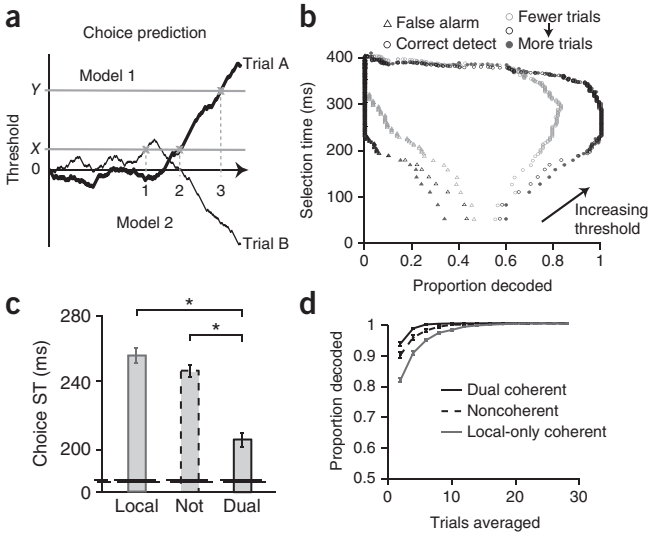

Figure 4 Accumulated log-likelihood model to detect movement choices. (**a**) Example choice classifications of two trials: trial A, belonging to model 1, and trial B to model 2. If the threshold is set to *X*, trial A is correctly classified as belonging to model 1; however, trial B is incorrectly classified, resulting in false alarm. The time that the trials cross the threshold is marked as the ST (times 1 and 2). Upon increasing the threshold to *Y*, both trials A and B are correctly classified. The ST is consequently increased as a result of the increased threshold. (**b**) Tradeoff between ST, the correct detection rate and false alarm rate. As the threshold of detection is increased, the false alarm rate decreases while the correct detection rate increases to an optimal level. Further increases in the threshold result in trials not reaching threshold and not being classified, reducing the correct detection rate. As the number of trials used in decoding increases, performance increases accordingly until saturation is reached. (**c**) Saturated STs for three different populations of dual-coherent (black solid), local-only coherent (gray solid) and noncoherent (dashed) neurons. Error bars indicate s.e.m. Neuron pools were of size 11. $*P < 0.05$. (**d**) Probability of correct classification when decoding movement choice from populations (mean ± s.e.m.).

specifically associated with how quickly visual input was processed to make a choice and not associated with differences in the timing of visual input.

The above analyses pool neurons from both banks of the IPS, so to ensure that the timing of activity was similar in each area, we compared the STs for each bank separately (**Supplementary Fig. 2**). Selection occurred at a similar time across the IPS (lateral, 205 ± 4 ms; medial, 201 ± 4 ms; $P = 0.47$, rank-sum test), so neurons on both banks were recruited together during look-reach decisions. The proportions of lateral and medial bank neurons with local and long-range SFC also did not differ significantly (**Supplementary Fig. 3**). The number of neurons for each population was as expected given the sample in the data set, with the exception of the long-range-only population (total number of MIP neurons in database, 42 of 72 = 58%; proportion of locally coherent MIP neurons, 30 of 53 = 57%; not significantly different from the whole proportion of the population, $P = 0.11$, binomial test). The same was true for the complement of LIP neurons ($P = 0.10$).

These results demonstrate that distributed neural ensembles in which neurons fire dual-coherently, in the lateral and medial banks of the PPC, are rapidly recruited. These dual-coherent neurons predict movement choices substantially before other groups of neurons.

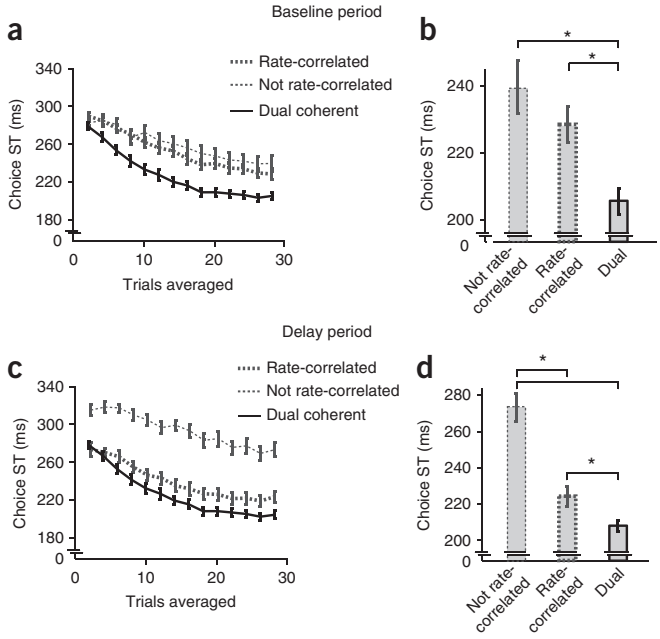

Neuronal ensembles defined by firing rate properties

Neuronal ensembles also display correlated firing rates. Ensembles of rate-correlated neurons may be preferentially recruited for decision-making. If so, groups of rate-correlated neurons should exhibit choice selectivity earlier than groups of coherent neurons. We defined a population of rate-correlated neurons (**Fig. 5a**,**b**). Our data set contained 60 neuron pairs, with 25 significantly rate-correlated in the baseline period (local, 22; long-range, 3; unique neurons that occur in the significant neuron pairs, 37) and 28 correlated in the early delay period (local, 23; long-range, 5; unique neurons, 45).

Coherent and rate-correlated labels were uncorrelated across neurons, suggesting separate underlying mechanisms. STs for both of the rate-correlated populations were significantly and substantially slower than for the dual-coherent population (baseline, 227 ± 6 ms; $P = 0.03$, rank-sum test; delay, 224 ± 6 ms; $P = 0.009$; **Fig. 5**). There was no significant difference between baseline-period groupings with and without rate correlations (no rate correlations, 240 ± 8 ms; $P = 0.35$), while delay-period rate-correlated neurons were significantly faster than those without rate correlations (no rate correlations, 277 ± 4 ms; $P = 7.1 \times 10^{-6}$). Therefore, rate-correlated ensembles were recruited during the early formation of movement plans, but temporally coherent ensembles were recruited even earlier.

Choice selectivity may be associated with neurons with higher overall levels of firing, not necessarily neurons with coherence (see **Supplementary Fig. 4**). To address this, we measured STs for groups of neurons defined according to the level of their baseline firing rate. High baseline firing ensembles had faster STs than low baseline firing ensembles (low, 289 ± 9 ms; high, 225 ± 9 ms; $P = 9.7 \times 10^{-6}$, rank-sum test) but were slower than dual-coherent neurons ($P = 0.019$, rank-sum test). Thus, the choice selectivity of coherent neuronal ensembles was not simply associated with groups of neurons that tended to fire more spikes (**Supplementary Figs. 5** and **6**). For the center-out task, dual-coherent neurons did not have larger differences in firing rate than local and noncoherent neurons (dual

Figure 5 STs for populations of neurons with and without rate correlations. (**a**) Baseline period. (**c**) Early delay period. (**b**,**d**) Bar graphs showing saturated STs. For all panels, neuron pools were of size 11. $*P < 0.05$. Mean ± s.e.m. are shown.

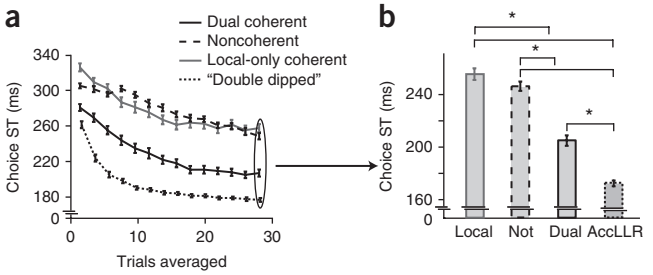

Figure 6 STs for the most selective groupings of neurons. (**a**) STs for a neural population defined by AccLLR selectivity ('double dipped'; gray). For comparison, populations defined by coherency are also shown. (**b**) Bar graph showing saturatd STs. For all panels, neuron pools were of size 11. $^*P < 0.05$. Mean ± s.e.m. are shown.

versus local, $P = 0.82$, dual versus noncoherent; $P = 0.54$; rank-sum test; **Supplementary Fig. 7**).

Greater firing during choice is likely to be a feature of choice selectivity because it allows larger differences in firing to exist for different choices. As expected, neurons with high firing rates during the delay period selected choices faster than those with low delay period firing rates (low delay ST = 288 ± 7 ms; high delay ST = 208 ± 4 ms; low versus high, $P < 1 \times 10^{-6}$; rank-sum test). Perhaps surprisingly, STs of neuronal ensembles with high delay period firing did not differ from STs of dual-coherent neurons (high versus dual; $P = 0.304$). Thus, coherence-related choice selectivity was similar in strength to selectivity associated with strong delay period activity.

Spike–spike coherence may also be used to define coherent ensembles, however only six neuron pairs exhibited significant beta frequency (20 Hz) coherence at a $P < 0.05$ significance level (permutation test), which would be expected by chance ($P = 0.08$, sign test). A similar lack of coherence was observed in the delay epoch ($n = 7$). Thus, identifying coherent ensembles depended on relating the spiking of neurons to LFP activity.

To assess how much choice information in neural firing was associated with the presence of coherence, we compared dual-coherent STs with the most choice-predictive ensembles in our data set. Neurons were ranked by how well they predict choices individually (AccLLR) and the most choice-predictive neurons were grouped, effectively 'double dipping' to extract the most information. This method yielded STs of 174 ± 2 ms after target onset with perfectly predicted choices (**Fig. 6**). The most choice-predictive ensembles were recruited significantly faster than dual-coherent ensembles ($P = 2.9 \times 10^{-7}$, rank-sum test); however, the dual-coherent ensemble was a relatively modest 30 ms slower, demonstrating that dual coherence is a good predictor of choice coding.

Controlling for the magnitude of coherence

Dual-coherent neurons tended to have stronger local coherence than local-only coherent neurons (**Fig. 2**). Fast STs in dual-coherent neurons may be due to the strength of local coherence and not the presence of both local and long-range coherence. Dual-coherent and local-only coherent neurons were divided into a more-local group with high local SFC and a less-local group with low local SFC, and the STs were calculated (**Fig. 7**). The ST for the dual-coherent ensemble with less-local SFC was significantly faster than the ST for the local-only ensemble with more-local SFC ($P = 1.2 \times 10^{-6}$, rank-sum test). Critically, local SFC magnitude for the more-local local-only coherent neurons was significantly greater than for the less-local dual-coherent neurons (**Fig. 7c**; $P = 0.0076$, rank-sum test).

We also grouped the dual-coherent population on the basis of the magnitude of long-range coherence. The ST for the more long-range SFC population was not significantly different from the ST for less long-range SFC (low, 202 ± 3 ms; high, 208 ± 7 ms; $P = 0.45$, rank-sum test). The role of dual-coherent ensemble in supporting fast ST was not associated with the magnitude of either the local or the long-range coherence. The early ST was associated with neurons that had both local and long-range coherence.

Controlling for errors in SFC labels

We performed analyses to demonstrate that coherence-based labels remained consistent across the trial and were not influenced by differences in firing rates across neurons. Dual-coherent neurons fired at higher rates, so timing analyses were re-estimated after randomly removing spikes from ('decimating') trials until firing rates across groups were matched (**Supplementary Fig. 4**). The results remained consistent with dual-coherent neuron firing rates separating earlier (**Supplementary Fig. 8a–d**) and being more informative earlier (**Supplementary Fig. 8e**; versus local, $P = 3.4 \times 10^{-6}$; versus noncoherent, $P = 1.9 \times 10^{-5}$; rank-sum test). Dual-coherent neurons from populations reclassified by decimating the firing rates before SFC estimation (**Supplementary Fig. 8f**; 201.8 ± 5.6 ms) also remained faster than local-only coherent ($P = 1.5 \times 10^{-7}$, rank-sum test) and noncoherent neurons ($P = 5.8 \times 10^{-7}$). Thus, the differences in STs were not due to the impact of differences in the overall firing rate across the populations.

Although SFC fluctuated in amplitude during the trial, neurons that showed coherence during the baseline were more likely to show coherence at other times in the trial than expected by chance (79% of coherent labels remained coherent), with the converse also being true for noncoherent labels (78%). We also recalculated the SFC labels and STs as we varied the test frequency. When the frequency was above 40 Hz, only a few neurons had significant coherence (**Fig. 2b–e**). For frequencies below 40 Hz, there was not much change in the classifications, with the ST for dual-coherent neurons not changing from what we

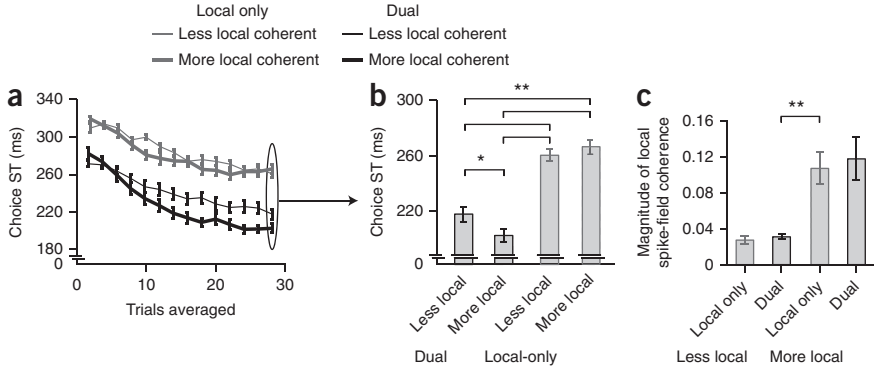

Figure 7 Controlling for the magnitude of coherence across populations. (**a**,**b**) STs for local-only coherent neurons and for dual neurons when separated by the magnitude of local coherence power. Neuron pools were of size 8. (**c**) Average local coherence magnitude for the dual-coherent and local-only coherent neurons when separated by the magnitude of local coherence. $^*P < 0.05$, $^{**}P < 0.01$. Mean ± s.e.m. are shown.

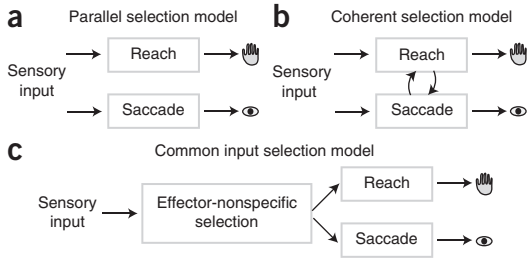

Figure 8 Selection models for multi-effector choices. (**a**) Parallel selection model where reach and saccade target selection occurs in parallel, dedicated systems that do not interact with each other. (**b**) Interacting selection model where selecting a reach-and-saccade movement depends on coordinating the activity of neurons across the reach and saccade systems. (**c**) Common input model where target selection for reaches and saccades results from common input to the parietal reach and saccade systems from a third, effector-nonspecific selection system.

observed at 20 Hz. This indicates that the effects shown depended on detecting beta-frequency coherence. Beta-band classification is desirable because it is unlikely to be affected by false-positive errors in SFC due to spike artifacts on same-electrode spike-field pairs. We compared same- and different-electrode SFC during the baseline (**Supplementary Fig. 9**), and although there was more coherence on same-electrode pairs at frequencies above 40 Hz, the coherence at 20 Hz was identical.

Finally, the differences we observed in mean firing rates across populations of coherent neurons suggested that coherence may reflect different cell types[35]. We recorded neurons with both broad and narrow spike widths with a dip at 500 µs ($P = 0.015$, Hartigan's dip test). A heterogeneous population of neurons with broad and narrow spike widths participated in each type of coherent activity (**Supplementary Fig. 10**), with dual-coherent neurons having significantly more narrow spike widths (60%; $P = 0.01$, binomial test).

These results demonstrate that distributed neural ensembles in which neurons fire dual-coherently, within the lateral and medial banks of the PPC, are rapidly recruited. These dual-coherent neurons predict movement choices substantially before other groups of neurons.

DISCUSSION

The firing rates of PPC neurons with distributed neuronal coherence predict look-reach movement choices earlier than those of other groups of neurons. Dual-coherent neurons, which fire spikes coherently with LFP activity on both banks of the IPS, contained a surprisingly large amount of information about the upcoming movement choice and were specific to movement selection. Furthermore, the firing rate selectivity that we observed indicates that selection may be driven by differences in the levels of firing by neurons interacting through coherent oscillatory activity. We next discuss implications of the results for models of reach and saccade selection before considering how coherence involves selection more broadly.

Parallel selection model

A simple model for reach and saccade target selection is the parallel selection model (**Fig. 8a**). Here, target selection for each movement takes place in a dedicated system and the two systems operate independently and in parallel[36]. The essential feature of this model is that reach and saccade selection do not interact with each other; the model, therefore, is consistent with our ability to make decisions for one effector or the other[37]. In the current experiments, we did not present single-effector movement choices but instead encouraged decisions for reaches and saccades to be made together. Choice-predictive dual coherence is evidence of functional coupling between reach and saccade selection and is not consistent with parallel selection.

Interacting selection models

Rather than occurring in parallel, selection may involve an effectively common selection stage due to interactions between the activity of neurons in the reach system and the saccade system[38,39] (**Fig. 8b**). These interactions could take the form of coherent patterns of neural activity. Our results support and constrain models of interacting selection and specifically support a model we term coherent selection.

The main prediction of interacting selection is that correlations in neural activity between the reach and saccade systems are associated with choice-predictive firing. Consistent with this, the most choice-predictive firing involved temporally precise patterns of spiking across both banks of the IPS. The relationship between temporally patterned firing and choice was present for each animal individually and survived efforts to control for variety of other confounding influences, such as the level of neural firing, the strength of neural coherence and the size of the neural ensemble used for decoding. Correlations on longer time scales in the firing rate (>100 ms) were present but were less choice-predictive. Therefore, our data support the hypothesis that making reach-saccade decisions involves interactions between the reach and saccade systems that these interactions take the form of coherent activity.

Coherence was not simply associated with visual input to the banks of the IPS. The visual selectivity of responses occurred at the same time in coherent and noncoherent populations. Choice selectivity appeared in both banks of the IPS at the same time, within milliseconds of the other area, and the earliest choice-specific signals only occurred in the coherent neurons some 10–20 ms after the onset of the visual response. These observations support a role for coherence in a choice process, not simply visual input or elevated firing, and show that selection processes in each area neither lead nor follow processes in the other.

Common input selection models

Other models of selection also involve coupling through common inputs to PPC from other potentially effector-nonspecific regions (**Fig. 8c**). Previous work has shown that reversibly inactivating neurons in either bank of the IPS creates spatially specific deficits in reward-guided choice tasks[20]. This implies that common input to the IPS alone does not select targets for both movements. However, interpreting these findings and distinguishing between common input and interacting selection involves establishing the connectivity and functional architecture of the large-scale decision network, not just the two posterior parietal regions we have studied.

Our work offers specific constraints on how common input can drive choice selective responses across the IPS. LFP activity reflects, in part, synaptic potentials near the recording electrode. If both banks of the IPS receive common input, LFP activity on each bank of the IPS is likely to reflect this. Choice-predictive dual coherence is, therefore, consistent with common input to PPC. However, choice-predictive dual coherence cannot result simply from the presence of common input to LFP activity on both banks. If inputs to the IPS are choice-specific, the magnitude of local coherence should be associated with increased choice selectivity. We found that neither the presence nor the magnitude of local coherence alone was associated with increased choice selectivity. The patterns of choice selectivity we observed across populations of dual-coherent neurons reveal a role for network interactions that must extend beyond common input alone. Further work involving causal manipulations

is needed to distinguish mechanisms involving common input from those involving direct and indirect interactions.

Bottom-up and top-down selection

We presented choice targets at random spatial locations trial by trial; therefore, initial visual input likely drove visual selectivity in a bottom-up manner. Conversely, blocks in which the circle or triangle targets were rewarded the most were interleaved and the resulting choices were sensitive to reward magnitudes; choice selectivity was thus likely due to top-down signals. Beta-frequency band activity has been recently linked to top-down control of visual attention[40]. Here, visual and choice selectivity offers a way to examine whether beta coherence is associated with top-down or bottom-up processes.

Visual selectivity occurred early and at the same time in both banks of the IPS and regardless of the presence of coherence, suggesting that common bottom-up input enters the IPS but that beta coherence is not involved in this process. Choice selectivity was present as early as 50 ms after target onset, and by ~200 ms, depending on the coherent ensemble, we could be 100% confident of predicting the choice. Behavioral work has shown that top-down influences can bias eye movement choices as early as 100 ms (ref. 41). Therefore, the initial choice selectivity appears consistent with top-down selection. Neurons from coherent and noncoherent ensembles eventually encoded the movement plan and did so with equal strength. Therefore, the relationship between distributed beta coherence was specific to the earliest period of selection, potentially at the time when the decision was being made.

Beta activity has been a focus of computational work suggesting a role in long-range processing because it is more robust to conduction delays than higher frequency activity[42]. Experimental evidence also indicates that beta activity may be particularly widespread across long-range neuronal circuits. Many studies indicate that beta activity in the frontal and parietal cortices is involved with and even necessary for decision making[26–28,43]. These studies and our own results indicate that the role of beta activity in decisions reflects top-down processing and may be related to the communication demands imposed by making a decision.

Long-range-only coherence and selection

A natural hypothesis is that long-range coherence is due to interactions that reflect how the decision signal is communicated between areas. Our results, however, show that choice-selective coherence does not specifically involve long-range coherence. In fact, long-range-only coherent neurons were strikingly poor at encoding the choice. Long-range-only coherent neurons were not associated with fast choice selectivity, and dual-coherent neurons with greater long-range coherence were not associated with faster choice selectivity. We conclude, therefore, that selection is associated with local coherence as much as long-range coherence. One explanation is that neurons whose activity is uncorrelated with local populations are not in a position to communicate relevant information about the movement choice to the long-range population. Long-range-only coherent neurons are, in a sense, disconnected from the local component of the decision mechanism. If this is true, it could explain why long-range-only coherent neurons are even less selective than neurons with no coherence. This is consistent with the idea that, if nearby neurons are not signaling together, then the signals that they send to other regions may also be less likely to correctly signal the choice. However, much larger samples of long-range-only neurons are necessary to draw strong conclusions.

Another important hypothesis is functional-anatomical and proposes that coherence involves neurons with particular anatomical properties[44]. For example, local coherence may be associated with interneurons and long-range-only coherence may be associated with pyramidal projection neurons. Our analysis of spike waveforms revealed a bimodal distribution of spike widths, consistent with the presence of at least two classes of cells in our data. Dual-coherent neurons fell roughly in even groups of putative interneuron (narrow spike width) and putative pyramidal (broad spike width) cells. This suggests that coherence is not necessarily a property of a given cell type. Particular cell types may be important in establishing the temporal patterning of coherent neuronal activity[45], but our data indicate that coherence is not itself restricted to particular cell types.

Caveats and concerns

We used two kinds of measures to analyze the temporal evolution of selection. Analyzing the separation in firing rate revealed when choice information was first present in the activity but did not indicate how accurately this separation could be detected. In contrast, our estimate of selection time controlled for detection accuracy and measured the time when selectivity can be detected with a given level of accuracy; namely, 100% (ref. 23). By showing that the speed and accuracy of the procedure did not improve when increasing the size of ensemble, we rigorously compared ensembles that differed in their coherency properties. Both measures of timing gave consistent results and likely captured similar aspects of neural function. This is because the early selectivity present in the separation of firing rates contributed to the selection time when choices could be accurately predicted.

Caveats should also be noted. First, and most importantly, the AccLLR procedure critically depended on fitting statistical models for the activity of neurons. We modeled activity with relatively flexible time-varying Poisson processes often used to characterize neural coding, but models that explicitly capture inter-trial variability may be more accurate[46]. Second, AccLLR is an efficient statistical procedure, but it is not intended to describe how neural activity in PPC is read out to select actions. The AccLLR procedure detected the decision by counting the number of spikes, not their timing. We chose to do this so that the signal timing results could not be due to temporal correlations. It is plausible that downstream brain areas read out the spiking activity using another algorithm—for example, one that incorporates spike timing and neural coherence.

Finally, the number of simultaneous recordings we could make limited our identification of coherent neurons. Errors in SFC classification could alter the neuronal ensembles, which could in turn alter the ST estimates. When detecting local SFC, false negatives should not be a concern because SFC is likely to be strongest when LFP activity is taken from the same electrode as spiking activity, and this very local LFP recording is always available. Our data (**Supplementary Fig. 9**) indicate that false positives are also not an issue, which is consistent with published work[47] that reports that spike contamination in the coherence at 20 Hz occurs only for neurons with wide spike widths, a signal-to-noise ratio greater than 16 and a spike rate greater than 20 spikes/s. Dual-coherent neurons in our data set had a smaller signal-to-noise ratio, narrower spikes and lower firing rates. False negatives in the long-range SFC cannot be ruled out, with the possibility that we have missed some dual-coherent neurons. More work is needed to address this concern. Despite these caveats, we note that our comparisons are based on several convergent measures that show that coherent ensembles in PPC are rapidly recruited when making decisions.

METHODS

Methods and any associated references are available in the online version of the paper.

Note: Any Supplementary Information and Source Data files are available in the online version of the paper.

ACKNOWLEDGMENTS

This work was supported, in part, by US National Institutes of Health (NIH) grant R01-MH087882 as part of the National Science Foundation (NSF)/NIH Collaborative Research in Computational Neuroscience Program, NIH R01-EY024067, NSF CAREER Award BCS-0955701, and the SUBNETS program sponsored by the US Defense Advanced Research Projects Agency Biological Technologies Office.

AUTHOR CONTRIBUTIONS

Y.T.W., B.P. and N.D.D. designed the experiments. Y.T.W., B.P., M.M.F. and Y.N. performed the experiments. Y.T.W., B.P., M.M.F., Y.N. and N.D.D. analyzed the data. Y.T.W., B.P. and N.D.D. wrote the manuscript.

COMPETING FINANCIAL INTERESTS

The authors declare no competing financial interests.

1. Lewis, J.W. & Van Essen, D.C. Corticocortical connections of visual, sensorimotor, and multimodal processing areas in the parietal lobe of the macaque monkey. *J. Comp. Neurol.* **428**, 112–137 (2000).
2. Johnson, P.B., Ferraina, S., Bianchi, L. & Caminiti, R. Cortical networks for visual reaching: physiological and anatomical organization of frontal and parietal lobe arm regions. *Cereb. Cortex* **6**, 102–119 (1996).
3. Van Der Werf, J., Jensen, O., Fries, P. & Medendorp, W.P. Neuronal synchronization in human posterior parietal cortex during reach planning. *J. Neurosci.* **30**, 1402–1412 (2010).
4. Konen, C.S., Mruczek, R.E.B., Montoya, J.L. & Kastner, S. Functional organization of human posterior parietal cortex: grasping- and reaching-related activations relative to topographically organized cortex. *J. Neurophysiol.* **109**, 2897–2908 (2013).
5. Marconi, B. *et al.* Eye-hand coordination during reaching. I. Anatomical relationships between parietal and frontal cortex. *Cereb. Cortex* **11**, 513–527 (2001).
6. Rozzi, S. *et al.* Cortical connections of the inferior parietal cortical convexity of the macaque monkey. *Cereb. Cortex* **16**, 1389–1417 (2006).
7. Cavada, C. & Goldman-Rakic, P.S. Posterior parietal cortex in rhesus monkey: II. Evidence for segregated corticocortical networks linking sensory and limbic areas with the frontal lobe. *J. Comp. Neurol.* **287**, 422–445 (1989).
8. Cavada, C. & Goldman-Rakic, P.S. Topographic segregation of corticostriatal projections from posterior parietal subdivisions in the macaque monkey. *Neuroscience* **42**, 683–696 (1991).
9. Schmahmann, J.D. & Pandya, D.N. Anatomical investigation of projections from thalamus to posterior parietal cortex in the rhesus monkey: a WGA-HRP and fluorescent tracer study. *J. Comp. Neurol.* **295**, 299–326 (1990).
10. Prevosto, V., Graf, W. & Ugolini, G. Cerebellar inputs to intraparietal cortex areas LIP and MIP: functional frameworks for adaptive control of eye movements, reaching, and arm/eye/head movement coordination. *Cereb. Cortex* **20**, 214–228 (2010).
11. Colby, C.L. Action-oriented spatial reference frames in cortex. *Neuron* **20**, 15–24 (1998).
12. Snyder, L.H., Batista, A.P. & Andersen, R.A. Coding of intention in the posterior parietal cortex. *Nature* **386**, 167–170 (1997).
13. Roitman, J.D. & Shadlen, M.N. Response of neurons in the lateral intraparietal area during a combined visual discrimination reaction time task. *J. Neurosci.* **22**, 9475–9489 (2002).
14. Sugrue, L.P., Corrado, G.S. & Newsome, W. T. Matching behavior and the representation of value in the parietal cortex. *Science* **304**, 1782–1787 (2004).
15. Platt, M.L. & Glimcher, P.W. Neural correlates of decision variables in parietal cortex. *Nature* **400**, 233–238 (1999).
16. Kubanek, J. & Snyder, L.H. Reward-based decision signals in parietal cortex are partially embodied. *J. Neurosci.* **35**, 4869–4881 (2015).
17. Liu, Y., Yttri, E.A. & Snyder, L.H. Intention and attention: different functional roles for LIPd and LIPv. *Nat. Neurosci.* **13**, 495–500 (2010).
18. Wilke, M., Kagan, I. & Andersen, R.A. Functional imaging reveals rapid reorganization of cortical activity after parietal inactivation in monkeys. *Proc. Natl. Acad. Sci. USA* **109**, 8274–8279 (2012).
19. Hwang, E.J., Hauschild, M., Wilke, M. & Andersen, R.A. Inactivation of the parietal reach region causes optic ataxia, impairing reaches but not saccades. *Neuron* **76**, 1021–1029 (2012).
20. Kubanek, J., Li, J.M. & Snyder, L.H. Motor role of parietal cortex in a monkey model of hemispatial neglect. *Proc. Natl. Acad. Sci. USA* **112**, E2067–E2072 (2015).
21. Hagler, D.J. Jr., Riecke, L. & Sereno, M.I. Parietal and superior frontal visuospatial maps activated by pointing and saccades. *Neuroimage* **35**, 1562–1577 (2007).
22. Dean, H.L., Hagan, M.A. & Pesaran, B. Only coherent spiking in posterior parietal cortex coordinates looking and reaching. *Neuron* **73**, 829–841 (2012).
23. Banerjee, A., Dean, H.L. & Pesaran, B. A likelihood method for computing selection times in spiking and local field potential activity. *J. Neurophysiol.* **104**, 3705–3720 (2010).
24. Womelsdorf, T. *et al.* Modulation of neuronal interactions through neuronal synchronization. *Science* **316**, 1609–1612 (2007).
25. Wang, X.-J. Neurophysiological and computational principles of cortical rhythms in cognition. *Physiol. Rev.* **90**, 1195–1268 (2010).
26. Haegens, S. *et al.* Beta oscillations in the monkey sensorimotor network reflect somatosensory decision making. *Proc. Natl. Acad. Sci. USA* **108**, 10708–10713 (2011).
27. Pesaran, B., Nelson, M.J. & Andersen, R.A. Free choice activates a decision circuit between frontal and parietal cortex. *Nature* **453**, 406–409 (2008).
28. Donner, T.H., Siegel, M., Fries, P. & Engel, A.K. Buildup of choice-predictive activity in human motor cortex during perceptual decision making. *Curr. Biol.* **19**, 1581–1585 (2009).
29. Pesaran, B., Pezaris, J.S., Sahani, M., Mitra, P.P. & Andersen, R.A. Temporal structure in neuronal activity during working memory in macaque parietal cortex. *Nat. Neurosci.* **5**, 805–811 (2002).
30. Salazar, R.F., Dotson, N.M., Bressler, S.L. & Gray, C.M. Content-specific fronto-parietal synchronization during visual working memory. *Science* **338**, 1097–1100 (2012).
31. Scherberger, H., Jarvis, M.R. & Andersen, R.A. Cortical local field potential encodes movement intentions in the posterior parietal cortex. *Neuron* **46**, 347–354 (2005).
32. Hagan, M.A., Dean, H.L. & Pesaran, B. Spike-field activity in parietal area LIP during coordinated reach and saccade movements. *J. Neurophysiol.* **107**, 1275–1290 (2012).
33. Bosman, C.A. *et al.* Attentional stimulus selection through selective synchronization between monkey visual areas. *Neuron* **75**, 875–888 (2012).
34. Gregoriou, G.G., Gotts, S.J., Zhou, H. & Desimone, R. High-frequency, long-range coupling between prefrontal and visual cortex during attention. *Science* **324**, 1207–1210 (2009).
35. Mitchell, J.F., Sundberg, K.A. & Reynolds, J.H. Differential attention-dependent response modulation across cell classes in macaque visual area V4. *Neuron* **55**, 131–141 (2007).
36. Sailer, U., Eggert, T. & Straube, A. Implications of distracter effects for the organization of eye movements, hand movements, and perception. *Prog. Brain Res.* **140**, 341–348 (2002).
37. de Lafuente, V., Jazayeri, M. & Shadlen, M.N. Representation of accumulating evidence for a decision in two parietal areas. *J. Neurosci.* **35**, 4306–4318 (2015).
38. Horstmann, A. & Hoffmann, K.-P. Target selection in eye-hand coordination: do we reach to where we look or do we look to where we reach? *Exp. Brain Res.* **167**, 187–195 (2005).
39. Vercher, J.L. & Gauthier, G.M. Oculo-manual coordination control: ocular and manual tracking of visual targets with delayed visual feedback of the hand motion. *Exp. Brain Res.* **90**, 599–609 (1992).
40. Bastos, A.M. *et al.* Visual areas exert feedforward and feedback influences through distinct frequency channels. *Neuron* **85**, 390–401 (2015).
41. Markowitz, D.A., Shewcraft, R.A., Wong, Y.T. & Pesaran, B. Competition for visual selection in the oculomotor system. *J. Neurosci.* **31**, 9298–9306 (2011).
42. von Stein, A. & Sarnthein, J. Different frequencies for different scales of cortical integration: from local gamma to long range alpha/theta synchronization. *Int. J. Psychophysiol.* **38**, 301–313 (2000).
43. Gould, I.C., Nobre, A.C., Wyart, V. & Rushworth, M.F.S. Effects of decision variables and intraparietal stimulation on sensorimotor oscillatory activity in the human brain. *J. Neurosci.* **32**, 13805–13818 (2012).
44. Gregoriou, G.G., Gotts, S.J. & Desimone, R. Cell-type-specific synchronization of neural activity in FEF with V4 during attention. *Neuron* **73**, 581–594 (2012).
45. Cardin, J.A. *et al.* Driving fast-spiking cells induces gamma rhythm and controls sensory responses. *Nature* **459**, 663–667 (2009).
46. Banerjee, A., Dean, H.L. & Pesaran, B. Parametric models to relate spike train and LFP dynamics with neural information processing. *Front. Comput. Neurosci.* **6**, 51 (2012).
47. Waldert, S., Lemon, R.N. & Kraskov, A. Influence of spiking activity on cortical local field potentials. *J. Physiol. (Lond.)* **591**, 5291–5303 (2013).

ONLINE METHODS

Experimental preparation. Two adult male rhesus macaques (*Macaca mulatta*) were used in this study (monkey C, 7.5 kg; monkey R, 6 kg). All surgical and animal care procedures were approved by the New York University Animal Care and Use Committee and were performed in accordance with US National Institute of Health guidelines for care and use of laboratory animals. Monkeys were socially pair-housed with one other male and were kept on a 12 h/12 h light/dark cycle. All experimental testing was completed during the light cycle under controlled-water access. Data collection and analysis were not performed blind to the conditions of the experiment.

We surgically implanted a head post to allow head restraint during behavioral training and electrophysiological recordings. After training, a square recording chamber, 16 × 16 mm inner dimensions, was attached to the skull and a craniotomy was made to gain access to the posterior parietal cortex. In monkey C, we targeted placement of the recording chamber and registered electrode recording locations to the cortical anatomy using a structural magnetic resonance image (MRI)-guided stereotaxic instrument (Brainsight, Rogue Research). The structural MRI was obtained with 0.5 mm isotropic voxels. MRI scans were not possible in monkey R due to the presence of iron in the soft tissue. Therefore, the recording chamber was placed according to stereotaxic coordinates over 7 P, 13 l and recording sites were functionally localized based on task responses and anatomically localized based on the depth of recordings from the cortical surface as indicated by transdural penetration of the recording electrode and the depth at which clearly identified action potentials were obtained.

Experimental hardware. The start and end positions of reaches were monitored via an acoustic touch-sensitive screen (ELO Touch Systems) and eye position was constantly monitored with an infrared optical eye tracking system sampling at 120 Hz (ISCAN). Visual stimuli were presented on an LCD monitor (Dell) placed directly behind the touch screen. The visual stimuli were controlled via custom LabView (National Instruments) software executed on a real-time embedded system (NI PXI-8184, National Instruments). Behavioral events were synchronized to neural recordings by placing a photodiode on the bottom corner of the monitor to detect visual stimulus events. On each experimental session, we inserted up to four glass-coated tungsten electrodes (Alpha Omega, 0.7–1.2 MΩ impedance at 1 kHz) through the dura mater into the IPS using a multielectrode motorized microdrive (NAN Instruments Ltd). Neural signals were amplified, low-pass filtered at 6 kHz and digitized at 30 kHz using 16 bits of resolution with the lowest significant bit equal to 0.1 μV (NSpike NDAQ System, Harvard Instrumentation Lab; ×10 gain headstage, Multichannel Systems). Recordings were referenced to the metal guide tube array resting on the dura in contact with the surface of the cortex above the recording sites.

Behavioral tasks. We trained two monkeys to perform four tasks in which they earned fluid rewards for making reaches to green targets, saccades to red targets and coordinated reach-and-saccades to yellow targets. During each experimental session, monkeys performed a center-out task and then three variants of a two-armed-bandit choice task. They were trained to reach using the arm contralateral to the hemisphere over which recording chamber was implanted (**Fig. 1b**).

The behavioral tasks were organized in two separate blocks of trials. In the first block of trials, 80 trials in duration, the monkeys performed a center-out task. In the second block of trials, 460 ± 295 trials (mean ± s.d.), the monkeys performed three choice tasks on randomly interleaved trials: a reach-and-saccade choice task, a saccade-only choice task and a reach-only choice task. Fluid rewards were delivered via an electronically controlled solenoid.

All four tasks shared the same set of initial events. The monkeys were trained to start each trial by placing their hands on two proximity sensors placed at waist height. A red and a green square were illuminated side-by-side at the center of the display (2° visual angle on a side, green on left). The monkeys then reached toward and touched the green square, and made a saccade to fixate the red square for a baseline period (500–800 ms, uniformly distributed).

In the center-out task, a yellow square target was then illuminated in the visual periphery (eccentricity 10° visual angle, one of eight possible locations) and the monkeys were trained to maintain fixation and touch for an instructed delay period of 1,000–1500 ms. After this time, the initial targets were extinguished, cueing the monkeys to reach and saccade to the target.

In the choice tasks, after this baseline period, two yellow targets (a triangle and circle) were presented, one placed 10° from the initial fixation and touch targets in the direction of the response field and the other placed 10° in the diametrically opposed direction. The shape of the target placed in the direction of the response field was randomly assigned each trial. The monkeys were instructed to maintain fixation and touch of the initial targets for a further 1,000–1,500 ms. At this point the initial fixation and touch targets were extinguished, cueing the monkeys to perform a reach and saccade to one of the two targets. After target presentation, touch and fixation were maintained for 300 ms, after which the monkey was given a fluid reward of volume determined by the target chosen. On a subset of trials, the yellow targets changed color to red (or green) 1,000–1,500 ms after the initial target onset. Each monkey maintained fixation and touch for a further 1,000–1,500 ms, after which the initial red (or green) square was extinguished, cueing the monkey to perform a saccade (or reach) to one of the two targets while maintaining touch (or fixation) of the initial green (or red) square. In this study, we analyzed data from reach-and-saccade task, reach task and saccade task types together, as only the neural activity immediately following target onset before the effector cue did not depend on the effector cue. We randomly interleaved reach-and-saccade, reach-only and saccade-only choice tasks trial by trial with probabilities of 0.24, 0.38 and 0.38, respectively. Both animals performed the same tasks and were not randomly assigned to a specific experimental grouping.

Neuronal recordings. We recorded neuronal activity from the medial and the lateral banks of the IPS in the PPC, ~5–10 mm below the cortical surface (**Fig. 1a**). On each experimental session, at least one electrode was lowered into each bank of the sulcus. Electrodes were positioned by a 2 × 2 square array of guide tubes, 2 mm on a side. The average separation between electrodes in the lateral bank was 1.9 ± 0.6 mm (mean ± s.d.); in the medial bank it was 2.1 ± 1 mm. Electrodes between banks of the IPS were separated on average by 2.6 ± 0.9 mm. Recordings were referenced to the metal guide tube array resting on the dura in contact with the surface of the cortex above the recording sites.

Spike preprocessing. We extracted spike waveforms from the neural recordings by first band-pass filtering the raw neural waveforms from 0.3 to 6.6 kHz (multitaper projection filter settings: time duration = 0.01 s, frequency bandwidth = 3,000 Hz, center frequency = 3.3 kHz) and then finding 1.6-ms duration sections of the filtered signal that crossed a threshold set at 3.5 s.d. below the mean filtered signal. We used a robust estimate of the s.d. Spike waveforms were projected into a three-dimensional principal component feature space on a moving 100-s time window. We used the *k*-means unsupervised clustering algorithm to over-cluster the spike waveforms. We then manually merged clusters that displayed clear separation from the multiunit noise cloud. Only time periods during the recording in which the single-unit cluster was clearly isolated from the multiunit noise cloud over the entire 100 s time window were accepted for further analysis. All clusters were verified by visual inspection off-line.

Criterion for unit acceptance. We entered spike recordings into the database only if they displayed significant task-related differences in firing rate. Specifically, we tested for differences between the firing rate in the choice task during the baseline and the firing rate during the 100-ms interval immediately following target onset (visual response) as well as during the 500-ms period subsequent (delay response; permutation test, $P < 0.05$). Statistical methods were not used to predetermine sample sizes; however, the sample sizes in this work are similar to those reported in previous publications.

LFP preprocessing. We obtained LFP activity by low-pass filtering the broadband recording at 400 Hz (multitaper projection filter settings: time duration = 0.025 s, frequency bandwidth = 400 Hz, center frequency = 0 Hz) and down-sampling the activity to 1 kHz from 30 kHz. To ensure that LFP activity was recorded from the banks of the IPS and not in between the sulci or in the white matter, we entered LFP recordings into the database only if they were made within 100 μm of a site that contained neuronal action potentials.

Response field analysis and single unit isolation. We analyzed neuronal response fields (RFs) measured during the center-out task to test whether RFs were sampled during the choice tasks with similar accuracy in the populations of dual-coherent, local-only, long-range-only and noncoherent neurons. We fit

the RF for each neuron by taking the firing rate during the delay period of the center-out task. A Von Mises function was fit to the response field for each cell. The Von Mises function models the response as a circular function centered about a mean angle with a width about the mean given by a concentration parameter. We measured the angular deviation between the placement of the choice targets and the center of the fitted response field and compared the deviation across each group of neurons. The angular deviation between the receptive field as mapped by the center-out task and fit with a Von Mises distribution and the placement of the choice target was checked to be not significantly different from 0 for all populations (dual, $P = 0.67$; local-only, $P = 0.5$; long-range-only, $P = 0.21$; noncoherent, $P = 0.84$). We also tested whether there was a significant difference in the degree of spatial tuning for each population of neurons during the instructed delay of the center-out task (**Supplementary Fig. 7**). The single-unit isolations during the recording were also controlled for to ensure that spike waveform signal-to-noise-ratios (mean waveform amplitude compared to the s.d. of the waveform noise) were different between populations (dual, 4.4 ± 0.4; local-only, 4.9 ± 0.4; long-range-only, 3.9 ± 0.5; noncoherent, 4.2 ± 0.4; dual versus local, $P = 0.38$; versus noncoherent, $P = 0.55$; versus long-range-only, $P = 0.35$; local versus noncoherent, $P = 0.13$; versus long-range-only, $P = 0.16$; noncoherent versus long-range-only, $P = 0.76$; rank-sum test).

Spike-field coherence analysis. We estimated spike-field coherence (SFC) using multitaper methods with 500-ms sliding windows with ±10 Hz frequency smoothing[48,49]. To test whether spike-field pairs had significant SFC, we tested the magnitude of the SFC at 20 Hz against a null hypothesis that there was no SFC using a permutation test (at least 10,000 permutations). We generated the null distribution for no SFC by randomly permuting the order of trials for the spiking data compared to the LFP data. SFC was tested during the baseline period 250 ms before the target onset cue to maximize the number of trials. We calculated SFC for spike-field pairs on electrodes within each area (local) and between areas (long-range). We also tested SFC during the delay period centered 250 ms after target onset. For the significant regions presented in the coherograms (**Fig. 2b–e**), we applied a cluster correction to correct for multiple comparisons[50]. To divide recordings into more-local and less-local coherence groups, we ranked recordings according to decreasing magnitude of the coherence and assigned the first 50% of recordings to the more-local coherence group and the last 50% to the less-local. The same procedure was used to assign recordings to more-long-range and less-long-range coherence groups. Neurons had two chances to be coherent with LFPs in each area. If the activity of a neuron was coherent with LFPs on one electrode but not another, the neuron was still classified as coherent.

Spike-spike analysis. We quantified the relationship between the spiking activity of two neurons by estimating the coherence between the two spike trains (the spike–spike coherence) and by estimating the Pearson correlation coefficient between the firing rates of the two neurons across trials (the spike-count correlation). We estimated spike–spike coherence and spike-count correlations using the same analysis parameters as we used for the SFC analysis. We also tested spike-count correlations during the delay period centered 250 ms after target onset.

Onset time analysis. We identified the onset of choice activity as the time after target onset that the firing rate of each neuron differed significantly before movement choices into and out of the RF. We did this by performing a Wilcoxon rank-sum test on each 50-ms time interval following the onset of the choice targets and detecting the first time when the results were significantly different at $P < 0.05$ using a two-sided test. Since this procedure involves making multiple comparisons, we corrected the significance of the Wilcoxon rank-sum tests by controlling for the false discovery rate.

Receiver-operating characteristic analysis. We compared how movement choice information in populations of neurons evolved in time moment by moment by performing a receiver-operating characteristic (ROC) analysis on the population average firing rate across sequential 50 ms time intervals and measuring the area under the ROC curve (AUC) at each time. The population average firing rate was calculated by averaging trials from either 12 randomly selected neurons from a population of neurons (**Fig. 3c,d**) or by averaging 5 randomly selected neurons from a population of neurons (**Supplementary Fig. 1a,b**). Neurons were selected without replacement. We performed statistical analyses of the moment-by-moment movement choice information by iterating the AUC calculations 20 times and constructing the empirical distribution function (EDF) of the AUC. To detect the onset of movement choice information, we performed a Wilcoxon rank-sum test on the AUC each 50-ms time interval and detecting the first time when the results were significantly different from chance (that is, AUC = 0.5; two-sided test) at $P < 0.05$. As in the onset time analysis, we corrected the significance of the Wilcoxon rank-sum tests by controlling for the false discovery rate.

Accumulated log-likelihood ratio model. To quantify the timing of neural signals across neural populations more rigorously, we used an accumulated log-likelihood ratio (AccLLR) method[23] derived from the literature on sequential design. We used the AccLLR method to determine when selectivity in the neural signals for two alternatives first emerged—the selection time (ST) of a neuron. The ST was defined by when the activity reached a threshold (**Fig. 4a**), with the speed–accuracy trade-off set by the level of the threshold (**Fig. 4b**). When the threshold was set low, detection was fast but inaccurate. As the threshold was raised, performance slowed but became more accurate. We estimated the ST while controlling the speed–accuracy trade-off by setting the threshold to the lowest level that gave perfect classification performance (100% correct detections and 0% false alarms).

In the AccLLR method, we defined a probabilistic model of the spiking activity for the two alternatives being tested. To determine the ST for a movement choice, the choice ST, we defined the two alternatives as movements into the RF and movements out of the RF. We also calculated visual ST by comparing the neural activity after the two peripheral targets appeared to the neural activity in the baseline period.

We modeled spiking as a time-varying Poisson process for each of the two alternatives. On each trial, neural activity for movements into or out of the RF was converted into a log-likelihood ratio that then accumulated in time. We combined the activity from the different neurons by assuming independence and averaging the likelihood across neurons. The detection performance across recordings from different populations was matched explicitly by varying the position of the threshold. The probability of correct decoding increased with increasingly large ensembles of neurons, changing STs. To avoid this confound, we measured decoding accuracy and ST using neuronal ensembles large enough that the results did not change when the number of neurons in the population was increased beyond a certain size. To increase ensemble sizes, we also averaged activity from different trials with the same movement choices. We call the process of testing populations of increasing size until there is no significant change saturating the decoding accuracy and STs. Once decoding accuracy and STs are saturated, performance will not change with larger ensembles from the same population and we have successfully controlled the speed–accuracy trade-off in the detection procedure.

For each of the models of spiking activity, we assumed that spike times are Poisson distributed with a time varying firing rate, $\lambda(t)$. For a given model at time bin $\Delta(t)$, the likelihood of spiking was given by

$$P\left(N(\Delta t)|\lambda(t)\right) = \frac{\exp\left(-\lambda(t)\Delta t\right)}{N(\Delta t)!}\left(\lambda(t)\Delta t\right)^{N(\Delta t)}$$

where $N\Delta(t)$ denotes the number of spikes that occurred in a short time (1 ms $\Delta(t)$ interval). The log-likelihood ratio, LLR(t), of a single spike train belonging to the two models being tested was given by

$$\begin{aligned}\mathrm{LLR}(t) &= \log\frac{P\left(\delta N(t)|\lambda_1(t)\right)}{P\left(\delta N(t)|\lambda_2(t)\right)} \\ &= \left(\lambda_2(t)-\lambda_1(t)\right)\Delta t + \delta N(t)\log\left(\frac{\lambda_1(t)}{\lambda_2(t)}\right)\end{aligned}$$

where $\delta N(t)$ denotes the spiking activity for each $\Delta(t)$ time interval starting at time t, with 1 representing a spike event and 0 representing no event.

The log-likelihood ratio can be calculated on a trial-average basis or averaged across an ensemble of neurons. Assuming that activity on each trial or for each cell is independent, the average log-likelihood ratio was given by

$$\mathrm{LLR}_{\mathrm{ave}}(t) = \sum_{i=1}^{N}\mathrm{LLR}_i(t)$$

doi:10.1038/nn.4210

Finally, the accumulated log-likelihood ratio was calculated by summing log-likelihoods (calculated from a single trial or multiple trials from a single or multiple cells) over time:

$$\mathrm{AccLLR}(t) = \sum_{t'=0}^{t} \mathrm{LLR}(t')$$

To test whether the ST of populations of neurons on the lateral bank differs significantly from the ST of populations of neurons on the medial bank, we measured the EDF of the saturated STs for each population. To do this, we randomly selected, without replacement, cell ensembles of size 10, 20, 30, 40 and 47 from each population and calculated STs for trial averages ranging from 2 to 28 trials. We obtained the EDF for each ST calculation by performing 40 iterations of this procedure and calculated the ST for each ensemble size by taking the mean ST across iterations. A Wilcoxon rank-sum test was used to test for significant differences between STs for different groups of neurons. To compare STs for neural ensembles of different coherent populations, we used the same procedure but with smaller ensembles of size 8 and 11 with trial averages ranging from 2 to 28. This was because there were fewer cells available in each coherent population. To ensure that the overall firing rate did not affect the STs, we performed control analyses by decimating firing rates so that the mean baseline firing rate was the same for all the groups of neurons being compared. We set the maximum accumulation time in the AccLLR analysis to 500 ms. The results did not change when the maximum accumulation time was reduced to 400 ms.

A **Supplementary Methods Checklist** is available.

48. Mitra, P.P. & Pesaran, B. Analysis of dynamic brain imaging data. *Biophys. J.* **76**, 691–708 (1999).
49. Jarvis, M.R. & Mitra, P.P. Sampling properties of the spectrum and coherency of sequences of action potentials. *Neural Comput.* **13**, 717–749 (2001).
50. Maris, E., Schoffelen, J.-M. & Fries, P. Nonparametric statistical testing of coherence differences. *J. Neurosci. Methods* **163**, 161–175 (2007).